Volume 3 | Number 9 | September 2015 | Pages 1247–1314

Biomaterials Science

www.rsc.org/biomaterialsscience

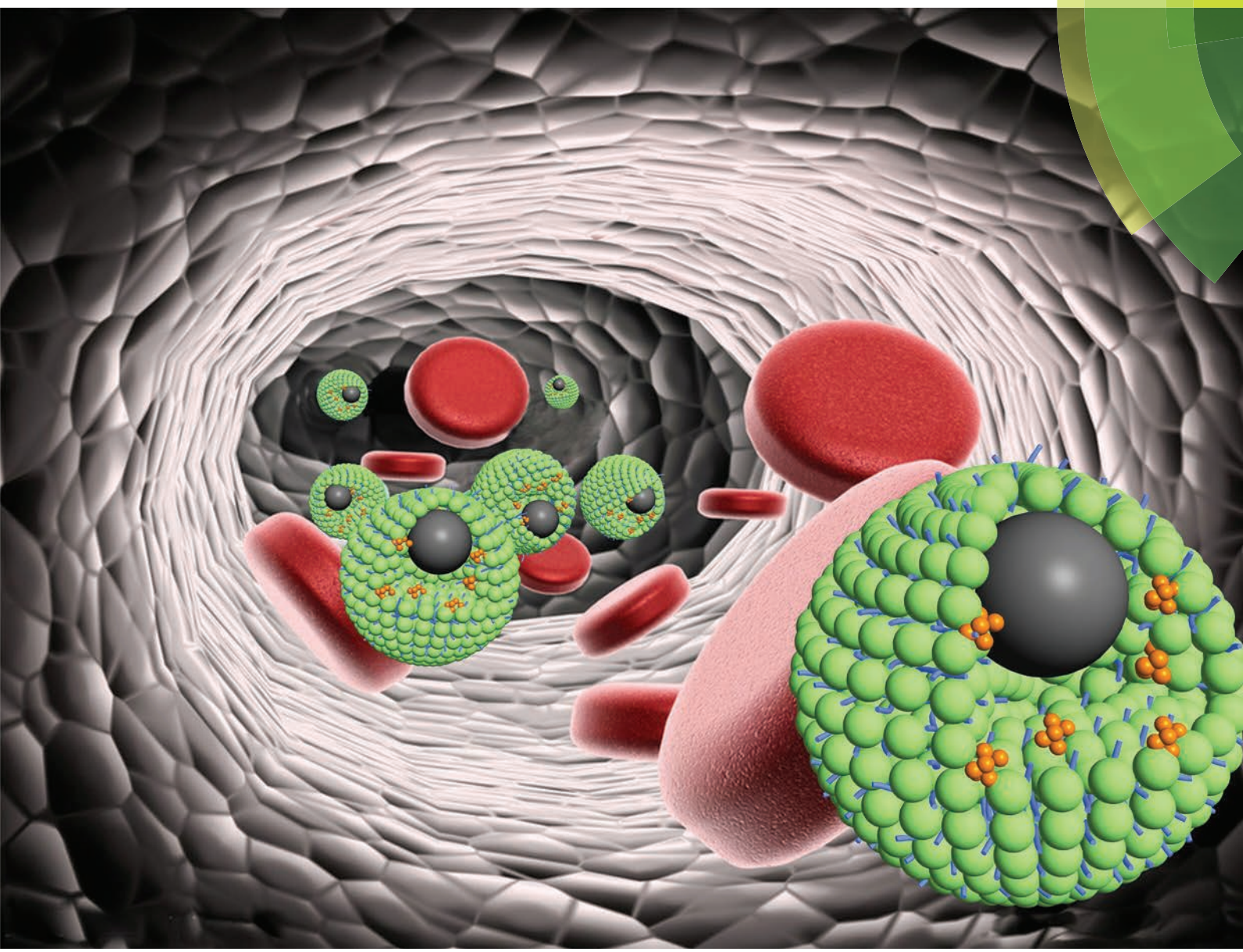

ROYAL SOCIETY OF CHEMISTRY

PAPER

Lu Li, Chungang Wang *et al.*

A combination of tri-modal cancer imaging and *in vivo* drug delivery by metal–organic framework based composite nanoparticles

iCeMS KYOTO UNIVERSITY WPI Research Center

Biomaterials Science

PAPER

View Article Online
View Journal | View Issue

Cite this: *Biomater. Sci.*, 2015, **3**, 1270

A combination of tri-modal cancer imaging and *in vivo* drug delivery by metal–organic framework based composite nanoparticles

Ruixin Bian,[a] Tingting Wang,[b] Lingyu Zhang,[a] Lu Li*[a] and Chungang Wang*[a]

Received 16th June 2015,
Accepted 20th July 2015

DOI: 10.1039/c5bm00186b

www.rsc.org/biomaterialsscience

Multifunctional Fe_3O_4@polyacrylic acid/Au nanoclusters/zeolitic imidazolate framework-8 nanoparticles (Fe_3O_4@PAA/AuNCs/ZIF-8 NPs) integrating tri-modal cancer imaging (magnetic resonance, computed X-ray tomography and fluorescence imaging) and chemotherapy into a single system were fabricated by using a facile, mild and reproducible strategy. The obtained NPs possess many merits including ultrahigh doxorubicin (DOX) loading capability (1.54 mg DOX per mg NPs), dual pH-responsive controlled drug release, tri-modal cancer imaging ability, facile magnetic separation and good biocompatibility. Importantly, the NPs exhibit low systematic toxicity and high antitumor therapy efficacy *in vivo* through tail vein injection. Furthermore, the achievement of *in vitro* tri-modal cancer cell imaging reveals the potential of Fe_3O_4@PAA/AuNCs/ZIF-8 NPs for cancer diagnosis and visualized-synergistic therapy. Taken together, Fe_3O_4@PAA/AuNCs/ZIF-8 NPs can be developed as a promising theranostic agent that combines multiple capabilities for cancer treatment.

1. Introduction

Zeolitic imidazolate frameworks (ZIFs) have attracted much attention in recent years for various applications including gas storage,[1–4] chemical separation,[5–7] catalysis,[8–11] sensing[12–14] and drug delivery[15] due to their fascinating properties, such as ultrahigh surface areas, abundant functionalities, exceptional thermal and chemical stabilities.[16,17] Both pure ZIFs and ZIF-based composites were developed as multifunctional materials with versatile and excellent performances.[18–21] Among these materials, ZIF-8 has been investigated as a drug delivery vehicle because it is stable in neutral and alkaline aqueous solution but decomposable quickly in acid solution,[22] which benefits for targeting tumor tissues whose extracellular pH value is lower compared to normal tissues.[23] The anticancer drug DOX has been readily incorporated into the ZIF-8 matrix,[24,25] whose pH-sensitive drug releasing property and excellent biocompatibility were manifested. However, to the best of our knowledge, there are few reports on ZIF-8-based multifunctional nanocomposites as a theranostic agent for simultaneous diagnostic and therapeutic applications.

The proposed design is the combination of cancer multi-modal imaging and chemotherapy in the ZIF-8 matrix to construct a multifunctional theranostic nanomedical platform, which can not only diagnose cancer and visualize nanoparticle (NP) accumulation by imaging but also simultaneously deliver drugs to facilitate the cancer treatment. Magnetic resonance (MR), X-ray computed tomography (CT) and optical imaging are common and powerful medical imaging tools for cancer diagnosis. However, single imaging technique has isolated strengths and inevitable weaknesses and is usually short of capabilities for comprehensive imaging.[26–28] In order to incorporate the superiorities and circumvent the limitations of different imaging techniques, the combination of multi-modal imaging is imperative.[29–34] Inspired by these, multifunctional Fe_3O_4@polyacrylic acid/gold nanoclusters/zeolitic imidazolate framework-8 NPs (Fe_3O_4@PAA/AuNCs/ZIF-8 NPs) were rationally designed to combine MR, CT and fluorescence tri-modal imaging, ultrahigh anticancer drug loading and dual pH-responsive drug release in a single system. Furthermore, *in vitro* and *in vivo* biocompatibility, *in vitro* imaging as well as *in vivo* tumor inhibition efficacy of the synthesized Fe_3O_4@PAA/AuNCs/ZIF-8 NPs were investigated in detail.

2. Experimental section

2.1 Chemicals and materials

Superparamagnetic iron oxide nanoparticles (Fe_3O_4 NPs) protected by oleic acid (OA) were obtained from Ocean Nano Tech. Hydrogen tetrachloroaurate ($HAuCl_4 \cdot 3H_2O$) was purchased

[a]*Faculty of Chemistry, Northeast Normal University, Changchun 130024, P. R. China. E-mail: wangcg925@nenu.edu.cn, lil106@nenu.edu.cn*
[b]*School of Chemistry and Engineering, Changchun University of Science and Technology, Changchun, 130022, P. R. China*

from Sigma (USA). Glutathione (GSH) was purchased from Beijing Dingguo Biotechnology. Doxorubicin hydrochloride (DOX) and polyacrylic acid (PAA, $M_w \approx 1800$) were purchased from Sigma (USA). Isopropyl alcohol, ammonia solution (2 M), and 2-methylimidazole (HMeIM) were purchased from Chengdu Kelong Chemical Reagent Company. $Zn(NO_3)_2{\cdot}6H_2O$ was purchased from Tianjin Fengchun Chemical Reagent Technologies Co., Ltd. Deionized water was used in all experiments.

2.2 Synthetic procedures of Fe_3O_4@PAA/AuNCs/ZIF-8 composite NPs

2.2.1 Synthesis of CTAB modification of Fe_3O_4 NPs. Monodisperse cetyltrimethylammonium bromide (CTAB) modified Fe_3O_4 NPs were prepared according to previous reports.[35,36] Typically, 800 μL of Fe_3O_4 NPs (25 nm in diameter, 10 mg mL^{-1}) capped with OA in chloroform were added in 16 mL, 0.2 mol mL^{-1} of CTAB aqueous solution under magnetic stirring at 32 °C for 30 min. Then the temperature was increased to 60 °C under continuous stirring. After 30 min, the solution was cooled to room temperature. Ultimately, CTAB modified Fe_3O_4 NPs were redispersed in 5 mL of deionized water after collecting by centrifugation.

2.2.2 Synthesis of Fe_3O_4@PAA core–shell NPs. On the basis of our previously published work,[37] 10 mL Fe_3O_4 NPs aqueous solution were added into a 250 mL flask under ultrasonic to form a suspension, to which 100 μL of PAA aqueous solution (0.2 g mL^{-1}) and 150 μL of $NH_3{\cdot}H_2O$ (2 M) were subsequently added. After 30 min of ultrasonic, 120 mL of isopropyl alcohol were dripped into the mixture under magnetic stirring to gain Fe_3O_4@PAA core–shell NPs.

2.2.3 Preparation of GSH capped AuNCs. GSH capped AuNCs were synthesized based on the previous report.[38] Briefly, 0.5 mL $HAuCl_4$ (20 mM) was added to 4.35 mL DI water and meanwhile 0.0046 g GSH was added to 0.15 mL DI water, and both were mixed under stirring at 25 °C for 5 min. The orange-emitting AuNCs were obtained after continuous stirring at 70 °C for 24 h, which were kept around 4 °C for further use.

2.2.4 Synthesis of Fe_3O_4@PAA/AuNCs/ZIF-8 composite NPs. 1 mL of the orange-emitting AuNCs solution was injected into the as-synthesized Fe_3O_4@PAA core–shell NPs solution after the pH value was adjusted to 8 with 0.1 M ammonia solution and stirred for 1 h. Afterwards, 500 μL isopropyl alcohol solution of $Zn(NO_3)_2$ (0.1 M) and HMeIM (0.1 M) was injected several times in turn at a 30 min interval under continuous stirring for 4 h at room temperature. After removing the unreacted species, the obtained eccentric Fe_3O_4@PAA/AuNCs/ZIF-8 composite NPs were washed with isopropyl alcohol and water respectively several times.

2.3 CT and MR imaging of Fe_3O_4@PAA/AuNCs/ZIF-8 NPs

Hounsfield units (HU), the CT numbers, of Fe_3O_4@PAA/AuNC/ZIF-8 NP samples with various concentrations (0, 27.28, 54.55, 81.83, 109.11, 136.38, 163.66, and 190.94 mg mL^{-1}) were determined using a SIEMENS SOMATOM Sensation 64 with a tube voltage of 120 kV, an electrical current of 280 mA, and a slice thickness of 1.0 mm. The presence of Au and Fe in the NPs was confirmed to be 0.97 wt% and 1.3 wt% respectively by using an inductively coupled plasma atomic emission spectrometer (ICP-AES).

The MR imaging experiment *in vitro* was performed using a 1.2 T MRI instrument (Shanghai Huantong Corporation HT-MRSI50-50KY). Dispersions of Fe_3O_4@PAA/AuNCs/ZIF-8 NPs with different concentrations (1.1365, 2.273, 3.4095, 4.5461, 5.6825, 6.819 mg mL^{-1}) were prepared and the corresponding values of transverse relaxation time T_2 were recorded. The T_2 relaxivity (r_2) was ascertained by a linear fitting of the inverse relaxation times as a function of Fe_3O_4@PAA/AuNCs/ZIF-8 NPs concentration.

2.4 CT and T_2-weight MR imaging in HepG-2 cells

1.0×10^5 mL^{-1} HepG-2 cells were seeded in a 24-well plate in IMDM medium followed by incubation with Fe_3O_4@PAA/AuNCs/ZIF-8 NPs with different concentrations (0, 0.56, 1.12, 2.25, 4.5, 8.1, 16.3, 32.7, 65.4 mg mL^{-1}) for 24 h at 37 °C. After being washed with phosphate-buffered saline (PBS) three times the cells were suspended in 0.2 mL PBS for CT and MR imaging. CT image parameters were as follows: thickness, 1.0 mm; pitch, 120 kV, 280 mA; field of view, 300 mm; gantry rotation time, 4.95 s. T_2-Weighted MR images of the cell solutions were acquired using a 1.2 T MR imaging instrument (Shanghai Huantong Corporation HT-MRSI50-50KY).

2.5 Fluorescence imaging in HepG-2 cells

In a similar procedure, HepG-2 cells were seeded onto glass cover slips in a 24-well plate within Iscove's modified Dulbecco's medium (IMDM) containing 10% fetal bovine serum (FBS) at 37 °C with 5% CO_2 for 24 h. Subsequently, the medium was replaced with a serum-free medium containing Fe_3O_4@PAA/AuNCs/ZIF-8 NPs (25 μg mL^{-1}). When incubated for 24 h, the dead cells and remaining Fe_3O_4@PAA/AuNCs/ZIF-8 NPs were removed by washing three times with PBS. The observations were performed using a confocal laser scanning microscope (CLSM) after the cells were sealed with a microscope glass slide.

2.6 Drug loading of Fe_3O_4@PAA/AuNCs/ZIF-8 NPs

UV-Vis spectroscopy was performed to monitor drug storage of the NPs. In a typical procedure, Fe_3O_4@PAA/AuNCs/ZIF-8 NPs (1 mg mL^{-1}, 1 mL) were mixed with an aqueous solution of DOX (10 mg mL^{-1} 190 μL) and stirred overnight. After magnetic separation by an external magnet and compared to the standard curve created previously by UV-Vis measurements at 480 nm, the DOX-loading efficiency (LE %) was gained, which was calculated by using eqn (1):

$$\mathrm{LE}\ (\%) = [(\mathrm{Abs}_{(\text{original DOX})} - \mathrm{Abs}_{(\text{remanent DOX})})/\mathrm{Abs}_{(\text{original DOX})}] \times 100\% \quad (1)$$

2.7 Drug release from DOX-loaded NPs

In vitro DOX release from DOX-loaded Fe_3O_4@PAA/AuNCs/ZIF-8 NPs was evaluated using a semipermeable dialysis bag

diffusion technique. 1 mL DOX-loaded NP solution was divided into two parts equally and dispersed in 0.5 mL of PBS (pH = 7.4 and 5.3) respectively after centrifuging. After the solution was transferred into pretreated semipermeable dialysis bags, the two bags were immersed into 3 mL of the corresponding PBS solution at 37 °C. At selected time intervals, the amount of DOX releasing from DOX-loaded NPs and moving into the solution was determined by using a fluorescence spectrophotometer with excitation at 479 nm and emission at 591 nm.

2.8 *In vitro* cytotoxicity against HepG-2 cells

The human liver cancer cells HepG-2 which were chosen to evaluate the cytotoxicity of Fe_3O_4@PAA/AuNCs/ZIF-8 NPs were grown into a 96-well plate and incubated at 37 °C with 5% CO_2 for 24 h. Serum-free medium containing Fe_3O_4@PAA/AuNCs/ZIF-8 NPs, DOX-loaded PAA@ZIF-8 NPs and free DOX with various concentrations was then added into the cells. 24 h later, 3-(4,5-dimethyl-thiazol-2-yl)-2,5-diphenyltetrazolium bromide (MTT) solution (20 μL, 5 mg mL^{-1}) was added. After incubation for 4 h, the medium was replaced with DMSO (150 μL) to dissolve the MTT formazan crystals. One row of the 96-well plate was used as a control with culture medium only and the absorbance was determined in a microplate reader at 490 nm. Cell viability was determined by using eqn (2):

$$\text{Cell viability } (\%) = \text{Abs}_{(\text{test cells})}/\text{Abs}_{(\text{control cells})} \times 100\% \quad (2)$$

2.9 About animal experiments

Balb/c mice were purchased from the Center for Experimental Animals, Jilin University (Changchun, China) and given access to food and water *ad libitum*. All the principles and procedures of animal experiments were in compliance with the relevant criteria and institutional guidelines of the National Regulation of China for Care and Use of Laboratory Animals and Regulations for the Administration of Affairs Concerning Laboratory Animals.

2.10 *In vivo* toxicity studies

Ten healthy Balb/c mice were divided into two groups randomly, one group of which was treated using Fe_3O_4@PAA/AuNCs/ZIF-8 NPs with a dose of 30 mg kg^{-1} to body weight by tail vein injection and the other of PBS as control. After that the mice weights were measured every other day. On the 13th day all the mice were euthanized and the main organs including heart, liver, spleen, and kidney were taken to examine the toxicity of Fe_3O_4@PAA/AuNCs/ZIF-8 NPs *in vivo*. These excised organs were embedded in 4% paraformaldehyde solution, sectioned and stained with hematoxylin and eosin (H&E) routinely for histological examination.

2.11 *In vivo* antitumor efficacy

The antitumor efficacy of Fe_3O_4@PAA/AuNCs/ZIF-8 NPs as a drug delivery system was investigated in Balb/c mice which bore tumors by subcutaneous injection of mouse hepatoma-22 (H-22) cells as described previously.[39,40] Briefly, H-22 cells, kindly gifted by Chemical biology laboratory of Changchun Institute of Applied Chemistry Chinese Academy of Sciences (Changchun, China), were suspended in physiological PBS and injected intraperitoneally into the mice for serial subcultivation. Then the mice with viable H-22 ascites tumors were sacrificed to withdraw the ascites, which were diluted with PBS afterwards to modulate the cell density at 1×10^7 cells per mL. The obtained ascites were injected subcutaneously to each mouse in the right leg with a dose of around 0.01 mL g^{-1} body weight. When the tumors had developed to 150–200 mm^3, fifteen mice were randomly divided into three groups, which were treated with DOX-loaded Fe_3O_4@PAA/AuNCs/ZIF-8 NPs, pure DOX and PBS as control by tail vein injection every three days. At the same time, the body weights of the mice were monitored and the injection dose of DOX was 4 mg kg^{-1} (equivalent nanoparticle dose was 2.6 mg kg^{-1}) body weight. The size of the tumor was measured with a vernier caliper. At the 13th day, all of the mice were executed to dissect the tumors whose weight were measured and recorded for the validation of therapeutic efficacy. Tumor growth inhibition ratio (IR) was defined by formula (3):

$$\text{Inhibition } (\%) = (w_c - w_t)/w_c \times 100\% \quad (3)$$

where w_c is the average tumor weight of the control group and w_t stands for the treated group. In addition, the photographs of the tumors from the mice of the three groups were also taken for a better comparison.

2.12 Characterization

Transmission electron microscopy (TEM) was performed on a JEOL-2100F transmission electron microscope under a 200 kV accelerating voltage. Field-Emission Scanning Electron Microscopy (FE-SEM) images and the energy dispersive X-ray (EDX) spectrum were obtained using an XL30 ESEM-FEG field-emission scanning electron microscope (FEI Co.). The HR-TEM characterization was performed with a TECNAI G2 F20 transmission electron microscope under a 200 kV accelerating voltage. X-ray powder diffraction (XRD) patterns were recorded on a D8 Focus diffractometer (Bruker) with Cu Kα radiation. Fourier transform infrared (FT-IR) spectra were recorded on a Magna 560 FT-IR spectrometer (Nicolet, USA). The magnetic measurement was carried out by using a superconducting quantum interference device magnetometer (SQUIDMPMS XL-7) with fields up to 1.5 T. Fluorescence spectra were recorded using an Eclipse fluorescence spectrophotometer (Varian, USA). N_2 adsorption/desorption measurements were performed by using an intelligent gravimetric analyser Autosorb-iQ (Quantachrome). UV-Vis absorption spectroscopy was performed on a U-3010 spectrophotometer (Hitachi, Japan). Confocal laser scanning microscopy (CLSM) was performed on an Olympus Fluoview FV1000. Inductively Coupled Plasma-Atomic Emission Spectrometry (ICP-AES) was performed with a Leeman ICP-AES Prodigy instrument. CT images were obtained by using a SIEMENS SOMATOM

Sensation 64, and the Hounsfield unit (HU) variations were determined by using a syngo CT 2009S instrument (Siemens, Berlin). T_2-Weighted MR images and the transverse relaxation time T_2 were obtained by using a 1.2 T MRI instrument (Shanghai Huantong Corporation HT-MRSI50-50KY).

3. Results and discussion

Scheme 1 illustrates the synthesis of Fe_3O_4@PAA/AuNCs/ZIF-8 composite NPs, which can be used for simultaneous tri-modal (MR, CT and fluorescence) bioimaging and cancer chemotherapy. Firstly, the OA-capped Fe_3O_4 NPs were transferred to CTAB modified Fe_3O_4 NPs. With the addition of PAA, ammonia solution, and isopropyl alcohol in sequence under ultrasonic, the PAA molecules assembled around Fe_3O_4 NPs to generate Fe_3O_4@PAA core–shell NPs. Subsequently, the discrete GSH capped AuNCs were added to form Fe_3O_4@PAA/AuNC NPs. Finally, the Fe_3O_4@PAA/GNCs/ZIF-8 composite NPs were obtained upon the addition of $Zn(NO_3)_2{\cdot}6H_2O$ and HMeIM. After the loading of DOX, the obtained DOX loaded Fe_3O_4@PAA/GNCs/ZIF-8 NPs with dual pH-responsive drug release are utilized as theranostic agents for *in vitro* tri-modal cancer cell imaging and *in vivo* cancer therapy.

Fig. 1A shows the TEM image of OA-capped Fe_3O_4 NPs with an average size of 20 nm, which were effectively transferred from the organic phase to the water phase by stabilizing surfactant CTAB. It can be seen that the Fe_3O_4 NPs are highly dispersed with no aggregations after transfer (Fig. 1A and B). After washing several times with water to remove the redundant CTAB, PAA aqueous solution, ammonia solution and isopropyl alcohol were added step by step and around 90 nm eccentric Fe_3O_4@PAA core–shell NPs were acquired owing to the variation of the interfacial energy of the system (Fig. 1C).[41] Upon the addition of the discrete GSH capped AuNCs, Fe_3O_4@PAA/AuNC NPs were successfully obtained, which may be attributed to the electrostatic interaction between the PAA and GSH. Subsequently, $Zn(NO_3)_2$ and HMeIM were added in sequence to obtain Fe_3O_4@PAA/AuNCs/ZIF-8 composite NPs with the size of about 130 nm, as shown in Fig. 1D. The high-resolution TEM (HR-TEM) image of the inset in Fig. 1D presents a part of a single Fe_3O_4@PAA/AuNC/ZIF-8 NP, revealing the existence of AuNCs in the NPs. The SEM image of Fe_3O_4@PAA/AuNCs/ZIF-8 NPs exhibits a relatively rough surface of the NPs, which may be composed of a large amount of small ZIF-8 NPs, forming the aggregated mesopores (Fig. 1E). The energy dispersive X-ray (EDX) spectrum demonstrates the elements in the as-prepared Fe_3O_4@PAA/AuNCs/ZIF-8 NPs including Fe, O, C, Au and Zn (Fig. 1F).

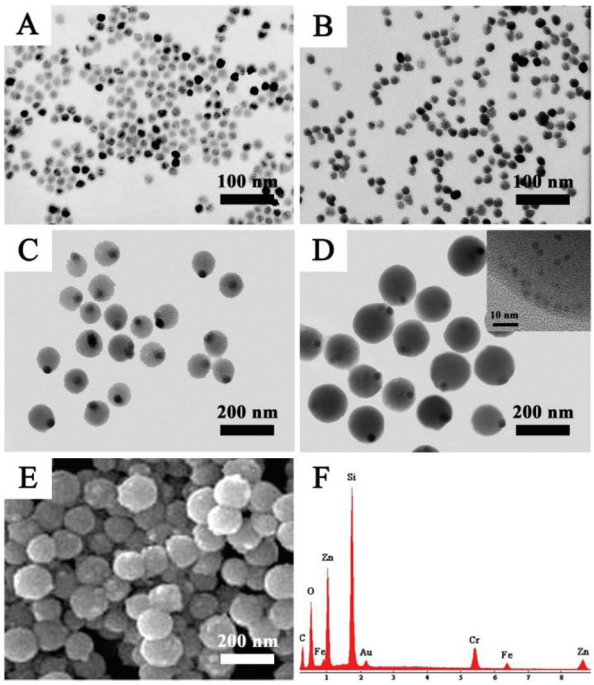

Fig. 1 TEM images of (A) OA-modified Fe_3O_4 NPs, (B) CTAB-stabilized Fe_3O_4 NPs, (C) eccentric Fe_3O_4@PAA core–shell NPs, and (D) Fe_3O_4@PAA/AuNCs/ZIF-8 core–shell NPs; (E) SEM image of Fe_3O_4@PAA/AuNCs/ZIF-8 core–shell NPs; (F) energy dispersive X-ray spectrum of Fe_3O_4@PAA/AuNCs/ZIF-8 NPs. Inset in (D) shows the HR-TEM image of part of a single Fe_3O_4@PAA/AuNC/ZIF-8 NP.

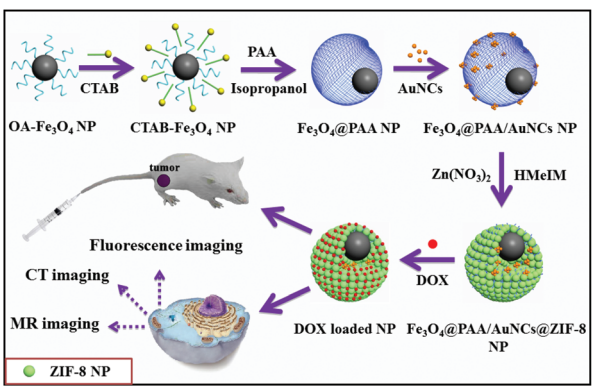

Scheme 1 Schematic illustration of the preparation of Fe_3O_4@PAA/AuNCs/ZIF-8 composite NPs for simultaneous tri-modal cancer imaging and chemotherapy.

FT-IR spectra and XRD (Fig. 2A and B) were performed to prove the successful coating of PAA and ZIF-8. In FT-IR spectroscopy (Fig. 2A), the peaks at 566 cm^{-1} in all the three characteristic curves are engendered by a Fe–O stretching mode, while peaks at 2921 cm^{-1} are responses to CTAB. The stretching vibration of C=O in the carboxyl group results in the peak at 1712 cm^{-1} and the peaks around 1550 cm^{-1} are associated with the shift of the C=O bands caused by the coordination of carboxyl with Zn^{2+} (curves b and c in Fig. 2A), indicating the existence of the PAA polymer in Fe_3O_4@PAA and Fe_3O_4@PAA/AuNCs/ZIF-8 NPs. Peaks in the 1100–1400 cm^{-1} region are assigned to C–N stretching of ZIF-8 (curve c in Fig. 2A).[25,42] The XRD pattern (Fig. 2B) verifies the presence of Fe_3O_4 and ZIF-8 in Fe_3O_4@PAA/AuNCs/ZIF-8 NPs for not only diffraction peaks marked with "*" which are in agreement with

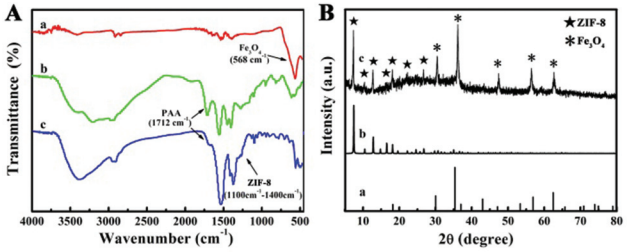

Fig. 2 (A) FT-IR spectra of (a) Fe_3O_4 NPs, (b) Fe_3O_4@PAA NPs and (c) Fe_3O_4@PAA/AuNCs/ZIF-8 NPs. (B) XRD spectra of (a) Fe_3O_4 NPs, JCPDS 88-0315, (b) simulated ZIF-8 NPs, and (c) Fe_3O_4@PAA/AuNCs/ZIF-8 NPs.

the standard XRD pattern of Fe_3O_4 powders (JCPDS 88-0315), but also those peaks marked with "*" which tally well with those of pure ZIF-8.[43]

To investigate the magnetic properties of the Fe_3O_4@PAA/AuNCs/ZIF-8 NPs, a superconducting quantum interference device (SQUID) magnetometer was used at 300 K and hysteresis loops were obtained in Fig. 3A. We found that the saturation magnetization value of Fe_3O_4@PAA/AuNCs/ZIF-8 NPs (8.2 emu g^{-1}) was evidently lower than that of Fe_3O_4 NPs (44.4 emu g^{-1}), which could be attributed to the nonmagnetic contribution of PAA/AuNC/ZIF-8 shells. The inset in Fig. 3A shows that the brown suspension of Fe_3O_4@PAA/AuNCs/ZIF-8 NPs gather quickly in the presence of an external magnet and leaves the solution transparent, which reveals the great potential of Fe_3O_4@PAA/AuNCs/ZIF-8 NPs for multiple biomedical applications, such as magnetically targeted drug delivery, MR and magnetic separation.

The fluorescence properties of Fe_3O_4@PAA/AuNCs/ZIF-8 NPs were examined in Fig. 3B. The obtained Fe_3O_4@PAA/AuNCs/ZIF-8 NPs show an obvious peak at 609.6 nm, which is typically consistent with that of discrete AuNCs from the photoluminescence (PL) spectra, indicating that the existence of ZIF-8 has no impact on the optical properties of AuNCs. It is worth noting that the fluorescence intensity of Fe_3O_4@PAA/AuNCs/ZIF-8 NPs is 2.5 times more intense than that of discrete AuNCs at the same concentration of AuNCs. This is because isopropanol and Zn^{2+} induced aggregation of the discrete AuNCs, causing the aggregation-enhanced fluorescence (AEF).[34] Isopropanol, as a weakly polar solvent, disrupted the hydration shell of Au(I)–thiolate complexes, resulting in charge neutralization and consequent aggregation of the complexes. Furthermore, the Zn^{2+}-induced aggregation exploited the high affinity of electrostatic and coordination interactions between Zn^{2+} and the monovalent carboxylic anions (from GSH) in the AuNCs.[38] Under UV light excitation, both the Fe_3O_4@PAA/AuNCs/ZIF-8 NPs and the discrete AuNCs emit orange colour while the Fe_3O_4@PAA/AuNCs/ZIF-8 NPs are much brighter than the discrete AuNCs (inset in Fig. 3B), which is another evidence for Fe_3O_4@PAA/AuNCs/ZIF-8 NPs with AEF properties.

In view of the presence of Au, which has a higher X-ray absorption coefficient than iodine agents of conventional CT,[28,44,45] Fe_3O_4@PAA/AuNCs/ZIF-8 NPs have been considered as a promising CT imaging contrast agent. Fig. 4A displays CT phantom images of Fe_3O_4@PAA/AuNCs/ZIF-8 NPs solution at various concentrations. The intensity of CT signals continuously enhance with the increase of the concentration of Fe_3O_4@PAA/AuNCs/ZIF-8 NPs. Hounsfield units (HU) treated as a function of the concentration of Fe_3O_4@PAA/AuNCs/ZIF-8 NPs exhibit a well-correlated linear relationship (R^2 = 0.9938), which can be described by the following equation: $y = 2.275x + 34.744$ (Fig. 4B). These results suggest that Fe_3O_4@PAA/AuNCs/ZIF-8 NPs are good candidates as positive CT imaging contrast agents.

Fe_3O_4@PAA/AuNCs/ZIF-8 NPs were also used as a transverse relaxation (T_2) contrast agent in MR imaging based on the superparamagnetic characteristics of the Fe_3O_4 cores, which can accelerate the transverse relaxation of water protons.[26,31] The iron content of Fe_3O_4@PAA/AuNCs/ZIF-8 NPs was determined using a ICP-AES and Fe_3O_4@PAA/AuNCs/ZIF-8 NP solutions with different concentrations were measured in a 1.2 Tesla magnetic field. As shown in Fig. 4C, Fe_3O_4@PAA/AuNCs/ZIF-8 NPs exhibit an evident attenuation effect on the MR

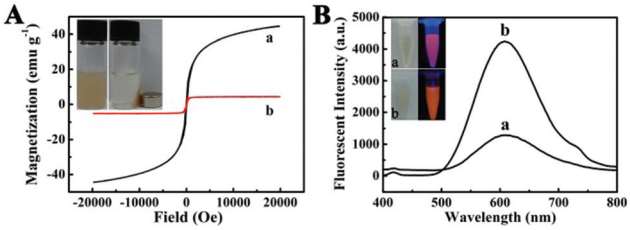

Fig. 3 (A) Hysteresis loop measurements of (a) Fe_3O_4 NPs and (b) Fe_3O_4@PAA/AuNCs/ZIF-8 NPs measured at 300 K, respectively. Insets: photographs of Fe_3O_4@PAA/AuNCs/ZIF-8 NP solutions without (left) and with (right) a magnet. (B) The PL spectrum of (a) discrete AuNCs (λ_{ex} = 365 nm) and (b) Fe_3O_4@PAA/AuNCs/ZIF-8 NPs (λ_{ex} = 365 nm). Insets: photographs of (a) discrete AuNCs and (b) Fe_3O_4@PAA/AuNCs/ZIF-8 NPs solution under room light (left) and UV light (right, λ_{ex} = 365 nm).

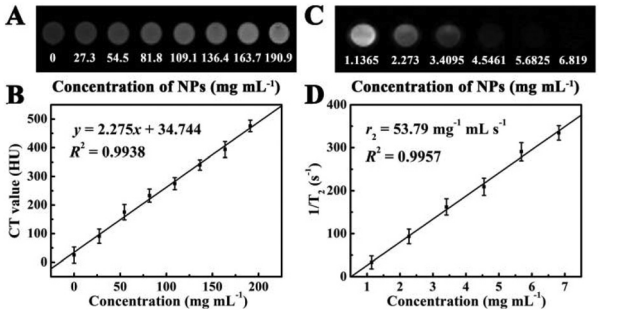

Fig. 4 (A) *In vitro* CT images of Fe_3O_4@PAA/AuNCs/ZIF-8 NPs with different concentrations (0–190.9 mg mL^{-1}). (B) Linear fitted CT values (HU) plot based on the HU of Fe_3O_4@PAA/AuNCs/ZIF-8 NPs at various concentrations (1.1365–6.819 mg mL^{-1}). (C) T_2 Weighted MRI of Fe_3O_4@PAA/AuNCs/ZIF-8 NPs at various concentrations. (D) Plot of inverse transverse relaxation time (1/T_2) *versus* NP concentrations, and the slope indicates the relaxivity value, r_2.

signal as the MR images darken with increasing concentrations of the NPs. The specific proton relaxivity value (r_2), the ratio of $1/T_2$ to the concentration of Fe_3O_4@PAA/AuNCs/ZIF-8 NPs, was computed through a linear regression curve fitting to be 53.79 mg^{-1} mL s^{-1} (Fig. 4D). The results indicate that Fe_3O_4@PAA/AuNCs/ZIF-8 NPs can serve as an efficient MR contrast agent to detect cancer. Moreover, the CT and MR images of HepG-2 cells treated with Fe_3O_4@PAA/AuNCs/ZIF-8 NPs with different concentrations were further measured. The CT signal intensity enhances visibly with the increasing concentration of the NPs (Fig. 5A) while the T_2 signal intensity reduces gradually (Fig. 5B), which is in accordance with the above-mentioned result of Fe_3O_4@PAA/AuNCs/ZIF-8 NPs solution.

Except for CT and MR imaging, Fe_3O_4@PAA/AuNCs/ZIF-8 NPs were employed for fluorescence imaging *in vitro*. CLSM images of HepG-2 cells incubated with Fe_3O_4@PAA/AuNCs/ZIF-8 NPs for 24 h at 37 °C under 5% CO_2 are shown in Fig. 5. Strong orange fluorescence emitted by AuNCs from the Fe_3O_4@PAA/AuNCs/ZIF-8 NPs is displayed in the cytoplasm regions of the cells (Fig. 5C), suggesting that the Fe_3O_4@PAA/AuNCs/ZIF-8 NPs are internalized by the cells *via* endocytosis rather than adsorption on the exterior of cells. Fig. 5D displays the corresponding bright-field fluorescence microscope image, in which the shape of the cells can be seen distinctly. The results clearly reveal the feasibility of the Fe_3O_4@PAA/AuNCs/ZIF-8 NPs as fluorescent nanoprobes for biomedical imaging. Taken together, the as-obtained Fe_3O_4@PAA/AuNCs/ZIF-8 NPs possess the potential as tri-modal contrast agents for simultaneous CT, MR and fluorescence imaging.

Nitrogen adsorption–desorption measurement was performed to investigate the specific surface area and pore nature of Fe_3O_4@PAA/AuNCs/ZIF-8 NPs. The adsorption–desorption isotherm and corresponding Barrett–Joyner–Halenda (BJH) pore size distribution are shown in Fig. 6A. The average pore size calculated from the isotherm is 3.8 nm, possibly due to the aggregation of small ZIF-8 NPs, which is in accordance with the SEM image (Fig. 1E). The Brunauer–Emmett–Teller (BET) surface area of the Fe_3O_4@PAA/AuNCs/ZIF-8 NPs is 603.5 m^2 g^{-1} and the total pore volume is 0.301 cm^3 g^{-1}. Such a high surface area and the mesoporous structure of Fe_3O_4@PAA/AuNCs/ZIF-8 NPs contribute to realize the high loading capacity of an anticancer drug.

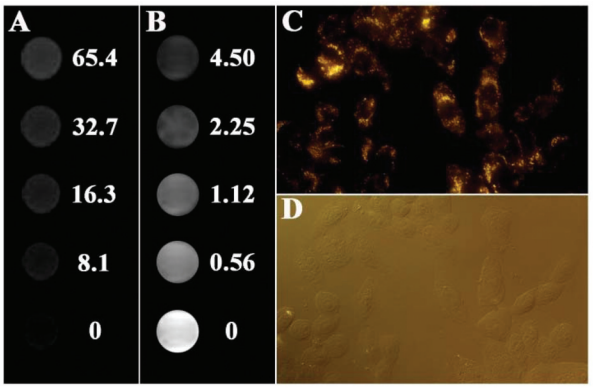

Fig. 5 (A) CT phantom images and (B) MR images of HepG-2 cells incubated with Fe_3O_4@PAA/AuNCs/ZIF-8 NPs with series of concentrations for 24 h; the concentrations are specified at right (mg mL^{-1}). (C) CLSM image of HepG-2 cells incubated with Fe_3O_4@PAA/AuNCs/ZIF-8 NPs for 24 h. (D) Corresponding bright-field contrast image.

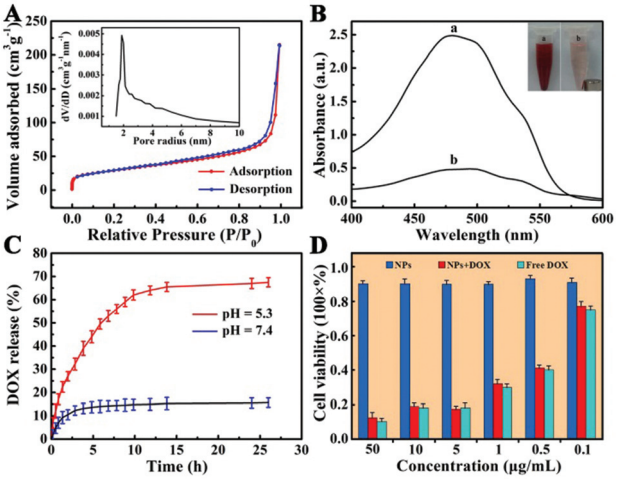

Fig. 6 (A) Nitrogen adsorption–desorption isotherm and the pore size distribution curve (inset) of Fe_3O_4@PAA/AuNCs/ZIF-8 NPs. (B) UV-Vis absorption spectra of DOX solutions before (a) and after (b) interacting with Fe_3O_4@PAA/AuNCs/ZIF-8 NPs; the inset is the photograph of DOX-loaded NPs without (a) and with (b) an external magnet for magnetic separation. (C) DOX-release profiles of DOX-loaded Fe_3O_4@PAA/AuNCs/ZIF-8 NPs measured in PBS at pH 5.3 and 7.4 at 37 °C. (D) *In vitro* cytotoxicity of Fe_3O_4@PAA/AuNCs/ZIF-8 NPs, DOX-loaded Fe_3O_4@PAA/AuNCs/ZIF-8 NPs and free DOX against HepG-2 cells at different concentrations.

Given the above facts, we chose DOX, a widely used water-soluble anticancer agent as a model drug, to estimate drug loading capacity of Fe_3O_4@PAA/AuNCs/ZIF-8 NPs. UV-Vis absorption spectra of the original DOX solution and the residual DOX in the supernatant after interacting with Fe_3O_4@PAA/AuNCs/ZIF-8 NPs were employed to determine the amount of DOX loaded into the NPs (Fig. 6B). The drug concentration in the solution reduces obviously according to the dramatic decrease of the absorption intensity in the spectra, which indicates the successful loading of DOX molecules into Fe_3O_4@PAA/AuNCs/ZIF-8 NPs. Surprisingly, the loading efficiency of DOX was calculated to reach 81.1% and an ultrahigh drug loading content was 1.54 mg DOX per mg Fe_3O_4@PAA/AuNCs/ZIF-8 NPs by mixing 190 μL initial DOX solution (10 mg mL^{-1}) with 1 mL NPs solution (1 mg mL^{-1}). Such ultrahigh loading capacity of DOX may be ascribed to the electrostatic interaction between the negatively charged carboxylic acid groups on PAA and the positively charged DOX as well as the coordination bonding of Zn(II)-DOX.[46] The inset in Fig. 6B shows that the DOX-loaded Fe_3O_4@PAA/AuNCs/ZIF-8 NPs solution can be separated by an external magnet due to the presence of Fe_3O_4 cores in the NPs. Meanwhile the color of

the solution changed from red to pale pink, further attesting the successful loading of DOX and the great potential of Fe_3O_4@PAA/AuNCs/ZIF-8 NPs for magnetically targeted drug delivery.

An efficient drug delivery system should have the ability of storing and delivering drug molecules as well as a sustained-release property. On account that the extracellular microenvironments of tumors are mildly acidic compared with those of normal tissues at the physiologically neutral pH,[47,48] dialysis bags with DOX-loaded Fe_3O_4@PAA/AuNCs/ZIF-8 NPs were immersed in PBS solution with different pH values (7.4 and 5.3) at 37 °C which imitated normothermia of humans for more than 24 h. As shown in Fig. 6C, the DOX-loaded NPs exhibit a property of sustained release, which benefits those clinical cases where a high initial dose of the drug is required followed by a relatively stable release of a smaller dose.[49] Furthermore, the rate of drug release is apparently pH dependent as 12.2% of the DOX is released within 15 min at pH 5.3, nevertheless, it takes 5 h to reach a comparable level at pH 7.4. In addition, the cumulative release amount of DOX attains 68% after 26.5 h in PBS buffer with pH 5.3 compared with 15% in PBS with pH 7.4, which would minimize side effects to normal tissues. The discrepant release profiles of DOX may result from two points: (1) the protonation of abundant carboxyl groups with the decrease in pH weakens the electrostatic interaction between DOX and PAA; (2) pH-sensitive dissolution properties of ZIF-8.[22,25,50] The results certify that Fe_3O_4@PAA/AuNCs/ZIF-8 NPs can be utilized as a dual pH-responsive controlled drug delivery vehicle for cancer chemotherapy.

Good biocompatibility is essential for further bio-applications likewise. Hence, *in vitro* and *in vivo* biological compatibility experiments were performed. Here we evaluated the cytotoxic effects of the Fe_3O_4@PAA/AuNCs/ZIF-8 NPs against HepG-2 cells by using standard MTT cell assays *in vitro*. Liver cancer cells HepG-2 were incubated with the Fe_3O_4@PAA/AuNCs/ZIF-8 NPs, DOX-loaded Fe_3O_4@PAA/AuNCs/ZIF-8 NPs and free DOX at different concentrations for 24 h and the corresponding cell viabilities are shown in Fig. 6D. Over 90% of the cells treated with the Fe_3O_4@PAA/AuNCs/ZIF-8 NPs survived even at a high concentration of 50 μg mL^{-1}, proving a low cytotoxicity of the NPs to cells. DOX-loaded Fe_3O_4@PAA/AuNCs/ZIF-8 NPs show a similar cytotoxic effect compared with the same concentration of DOX, demonstrating that Fe_3O_4@PAA/AuNCs/ZIF-8 NPs are an efficient drug delivery carrier.

To further investigate the systematic toxicity of Fe_3O_4@PAA/AuNCs/ZIF-8 NPs *in vivo*, histological assessment of the tissues of two mice groups was undertaken. One group was intravenously injected Fe_3O_4@PAA/AuNCs/ZIF-8 NPs *via* the tail vein while the other group was injected PBS as control. After 13 days all the mice were euthanized and the main organs were removed. As shown in Fig. 7, the organs, including heart, liver, spleen and kidney, taken from the injected mice were normal compared with those from the control group. These results imply that Fe_3O_4@PAA/AuNCs/ZIF-8 NPs possess good biocompatibility, making it promising for cancer theranostics.

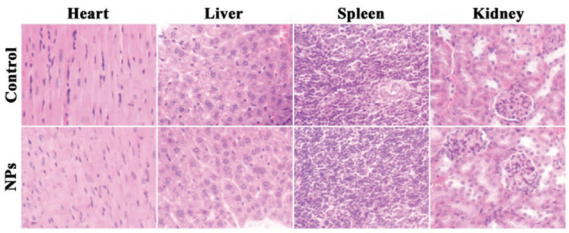

Fig. 7 Hematoxylin and eosin (H&E) stained images of major organs from healthy mice treated with Fe_3O_4@PAA/AuNCs/ZIF-8 NPs solution and PBS as control for 13 days.

To verify the capability of Fe_3O_4@PAA/AuNCs/ZIF-8 NPs as an efficient drug delivery vehicle for *in vivo* tumor inhibition, therapeutic efficacy for hepatocarcinoma was estimated using a H-22 xenograft model manufactured by grafting H-22 cells onto the leg of Balb/c mice. Fifteen mice with tumors were divided into three groups randomly and treated with PBS as control, free DOX and DOX-loaded Fe_3O_4@PAA/AuNCs/ZIF-8 NPs (DOX-NPs), respectively. A series of experiments and calculations on the tumor morphology, the tumor weight, the weight of the mice and the average tumor inhibition rate were carried out and the results are shown in Fig. 8. The intravenous treatments were given to these mice through tail vein injection every three days and body weights of the mice were monitored simultaneously. During the experiments the weight of the mice increases steadily and the variation of average body weight in the three groups of mice is similar (Fig. 8A). All of the mice were sacrificed at the 13th day to excise and weigh the tumors, then the weight of tumors and inhibition rates

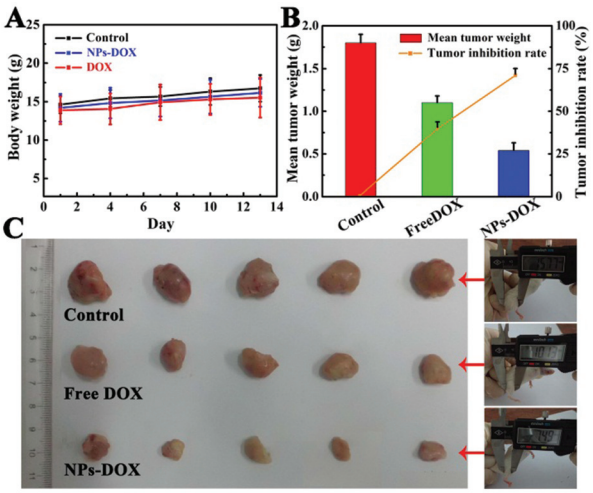

Fig. 8 (A) Changes in body weights of three groups of Balb/c mice during the 13 days from the first intravenous injection with PBS as control, free DOX and DOX-loaded Fe_3O_4@PAA/AuNCs/ZIF-8 NPs respectively. (B) Mean tumor weight and the average tumor inhibition rate of each group. (C) Photographs of excised tumors from euthanized mice in the three groups.

were obtained. It can be visibly seen in Fig. 8C that the tumor sizes of DOX-NPs and free DOX groups are smaller compared to those of the control group, manifesting tumor inhibition for both groups. Furthermore, according to the mean tumor weight ranging from 1.8 g in the control group and 1.1 g in the DOX group to 0.54 g in the DOX-NP group, a remarkable average inhibition rate is calculated to be approximately 70% in the DOX-NP group, much higher than 38.6% in the DOX group (Fig. 8B). The enhanced tumor inhibition of DOX-NPs is prominent, which may be ascribed to the accumulation of DOX-NPs in the intra-tumor space due to the effective enhanced permeability and retention (EPR) effect and *in vivo* sustained DOX release from DOX-NPs.[39,51] From the data above, conclusion is drawn that the Fe_3O_4@PAA/AuNCs/ZIF-8 NPs can effectively transmit anticancer drugs to the tumor site and help to suppress the growth of tumor.

4. Conclusion

In summary, multifunctional Fe_3O_4@PAA/AuNCs/ZIF-8 NPs as a theranostic agent have been successfully constructed for the first time *via* a facile, mild and reproducible method. It is worth noting that the obtained Fe_3O_4@PAA/AuNCs/ZIF-8 NPs are of great value in applications for simultaneous anticancer drug delivery and tri-modal (MR, CT and fluorescence) imaging. Furthermore, the as-fabricated NPs possess an ultra-high loading capacity of DOX (1.54 g DOX g^{-1} NPs) and dual pH-responsive controlled drug release properties. *In vitro* cytotoxicity studies and *in vivo* histological examinations reflect that Fe_3O_4@PAA/AuNCs/ZIF-8 NPs are biocompatible. Importantly, *in vivo* antitumor efficacy indicates that the Fe_3O_4@PAA/AuNCs/ZIF-8 NPs can suppress tumor growth effectively by delivering drug into the tumor site *via* the EPR effect. Furthermore, the achievement of *in vitro* tri-modal imaging reveals the potential of Fe_3O_4@PAA/AuNCs/ZIF-8 NPs for cancer diagnosis and visualized-synergistic therapy. Therefore, such multifunctional NPs have a great potential for simultaneous tri-modal imaging diagnostics and cancer chemotherapy as an effective dual pH-responsive drug delivery system.

Acknowledgements

This work was supported by the National Natural Science Foundation of China (Grant No. 21173038, 21401013 and 21301027), the Natural Science Foundation and Science and Technology Development Planning of Jilin Province (20130522136JH, 20130521010JH and 20140520088JH), the Program for New Century Excellent Talents in University (NCET-13-0720), the Specialized Research Fund for the Doctoral Program of Higher Education (New Teachers, 20132216120002) and the National Hi-Technology Research and Development Program (863 Program) (No. 2013AA032204 and 2014DFA31740) and Jilin Provincial Key Laboratory of Micro-Nano Functional Materials (Northeast Normal University) and Postdoctoral Science Foundation of China (2014M551155).

Notes and references

1 B. A. Al-Maythalony, O. Shekhah, R. Swaidan, Y. Belmabkhout, I. Pinnau and M. Eddaoudi, *J. Am. Chem. Soc.*, 2015, **137**, 1754.
2 L. J. Murray, M. Dinca and J. R. Long, *Chem. Soc. Rev.*, 2009, **38**, 1294.
3 T. Jose, Y. Hwang, D. W. Kim, M. I. Kim and D. W. Park, *Catal. Today*, 2015, **245**, 61.
4 K. Sumida, D. L. Rogow, J. A. Mason, T. M. McDonald, E. D. Bloch, Z. R. Herm, T. H. Bae and J. R. Long, *Chem. Rev.*, 2012, **112**, 724.
5 S. Hwang, W. S. Chi, S. J. Lee, S. H. Im, J. H. Kim and J. Kim, *J. Membr. Sci.*, 2015, **480**, 11.
6 J. R. Li, J. Sculley and H. C. Zhou, *Chem. Rev.*, 2012, **112**, 869.
7 J. R. Li, R. J. Kuppler and H. C. Zhou, *Chem. Soc. Rev.*, 2009, **38**, 1477.
8 P. Hu, J. V. Morabito and C. K. Tsung, *ACS Catal.*, 2014, **4**, 4409.
9 A. Corma, H. García and F. X. Llabrés i Xamena, *Chem. Rev.*, 2010, **110**, 4606.
10 H. Liu, L. Chang, L. Chen and Y. Li, *J. Mater. Chem. A*, 2015, **3**, 8028.
11 M. Yurderi, A. Bulut, M. Zahmakiran, M. Gülcan and S. Özkar, *Appl. Catal., B*, 2014, **160–161**, 534.
12 Z. Yuan, Y. Du, Y. T. Tseng, M. Peng, N. Cai, Y. He, H. T. Chang and E. S. Yeung, *Anal. Chem.*, 2015, **87**, 4253.
13 L. E. Kreno, K. Leong, O. K. Farha, M. Allendorf, R. P. Van Duyne and J. T. Hupp, *Chem. Rev.*, 2012, **112**, 1105.
14 C. He, K. Lu and W. Lin, *J. Am. Chem. Soc.*, 2014, **136**, 12253.
15 J. Zhuang, C. H. Kuo, L. Y. Chou, D. Y. Liu, E. Weerapana and C. K. Tsung, *ACS Nano*, 2014, **8**, 2812.
16 B. Chen, Z. Yang, Y. Zhu and Y. Xia, *J. Mater. Chem. A*, 2014, **2**, 16811.
17 S. R. Venna, J. B. Jasinski and M. A. Carreon, *J. Am. Chem. Soc.*, 2010, **132**, 18030.
18 L. H. Wee, Y. Li, K. Zhang, P. Davit, S. Bordiga, J. Jiang, I. F. J. Vankelecom and J. A. Martens, *Adv. Funct. Mater.*, 2015, **25**, 516.
19 Y. Cui, Y. Yue, G. Qian and B. Chen, *Chem. Rev.*, 2012, **112**, 1126.
20 D. Bradshaw, A. Garai and J. Huo, *Chem. Soc. Rev.*, 2012, **41**, 2344.
21 A. Bétard and R. A. Fischer, *Chem. Rev.*, 2012, **112**, 1055.
22 C. Y. Sun, C. Qin, X. L. Wang, G. S. Yang, K. Z. Shao, Y. Q. Lan, Z. M. Su, P. Huang, C. G. Wang and E. B. Wang, *Dalton Trans.*, 2012, **41**, 6906.
23 L. Xing, H. Zheng, Y. Cao and S. Che, *Adv. Mater.*, 2012, **24**, 6433.
24 I. B. Vasconcelos, T. G. d. Silva, G. C. G. Militao, T. A. Soares, N. M. Rodrigues, M. O. Rodrigues,

N. B. d. Costa, R. O. Freire and S. A. Junior, *RSC Adv.*, 2012, **2**, 9437.
25 H. Ren, L. Zhang, J. An, T. Wang, L. Li, X. Si, L. He, X. Wu, C. Wang and Z. Su, *Chem. Commun.*, 2014, **50**, 1000.
26 N. Lee and T. Hyeon, *Chem. Soc. Rev.*, 2012, **41**, 2575.
27 H. B. Na, I. C. Song and T. Hyeon, *Adv. Mater.*, 2009, **21**, 2133.
28 J. Michaelis, C. Hettich, J. Mlynek and V. Sandoghdar, *Nature*, 2000, **405**, 325.
29 B. Liu, C. Li, P. a. Ma, Y. Chen, Y. Zhang, Z. Hou, S. Huang and J. Lin, *Nanoscale*, 2015, **7**, 1839.
30 N. Lee, H. R. Cho, M. H. Oh, S. H. Lee, K. Kim, B. H. Kim, K. Shin, T. Y. Ahn, J. W. Choi, Y. W. Kim, S. H. Choi and T. Hyeon, *J. Am. Chem. Soc.*, 2012, **134**, 10309.
31 J. E. Lee, N. Lee, H. Kim, J. Kim, S. H. Choi, J. H. Kim, T. Kim, I. C. Song, S. P. Park, W. K. Moon and T. Hyeon, *J. Am. Chem. Soc.*, 2010, **132**, 552.
32 L. Zhang, W. F. Dong and H. B. Sun, *Nanoscale*, 2013, **5**, 7664.
33 H. Xing, W. Bu, S. Zhang, X. Zheng, M. Li, F. Chen, Q. He, L. Zhou, W. Peng, Y. Hua and J. Shi, *Biomaterials*, 2012, **33**, 1079.
34 X. Wu, C. Li, S. Liao, L. Li, T. Wang, Z. Su, C. Wang, J. Zhao, C. Sui and J. Lin, *Chem. – Eur. J.*, 2014, **20**, 8876.
35 J. Kim, H. S. Kim, N. Lee, T. Kim, H. Kim, T. Yu, I. C. Song, W. K. Moon and T. Hyeon, *Angew. Chem., Int. Ed.*, 2008, **47**, 8438.
36 L. Chen, L. Li, T. Wang, L. Zhang, S. Xing, C. Wang and Z. Su, *Nanoscale*, 2014, **6**, 6603.
37 L. Li, L. Zhang, S. Xing, T. Wang, S. Luo, X. Zhang, C. Liu, Z. Su and C. Wang, *Small*, 2013, **9**, 825.
38 Z. Luo, X. Yuan, Y. Yu, Q. Zhang, D. T. Leong, J. Y. Lee and J. Xie, *J. Am. Chem. Soc.*, 2012, **134**, 16662.
39 C. Li, D. Yang, P. A. Ma, Y. Chen, Y. Wu, Z. Hou, Y. Dai, J. Zhao, C. Sui and J. Lin, *Small*, 2013, **9**, 4150.
40 H. Xiao, H. Song, Y. Zhang, R. Qi, R. Wang, Z. Xie, Y. Huang, Y. Li, Y. Wu and X. Jing, *Biomaterials*, 2012, **33**, 8657.
41 L. Li, T. Wang, L. Zhang, Z. Su, C. Wang and R. Wang, *Chem. – Eur. J.*, 2012, **18**, 11417.
42 H. J. Lee, W. Cho and M. Oh, *Chem. Commun.*, 2012, **48**, 221.
43 L. He, T. Wang, J. An, X. Li, L. Zhang, L. Li, G. Li, X. Wu, Z. Su and C. Wang, *CrystEngComm*, 2014, **16**, 3259.
44 O. Rabin, J. Manuel Perez, J. Grimm, G. Wojtkiewicz and R. Weissleder, *Nat. Mater.*, 2006, **5**, 118.
45 C. R. Patra, R. Bhattacharya, D. Mukhopadhyay and P. Mukherjee, *Adv. Drug Delivery Rev.*, 2010, **62**, 346.
46 H. Zheng, L. Xing, Y. Cao and S. Che, *Coord. Chem. Rev.*, 2013, **257**, 1933.
47 Y. Zhao, L. N. Lin, Y. Lu, S. F. Chen, L. Dong and S. H. Yu, *Adv. Mater.*, 2010, **22**, 5255.
48 L. Chen, L. Li, L. Zhang, S. Xing, T. Wang, Y. A. Wang, C. Wang and Z. Su, *ACS Appl. Mater. Interfaces*, 2013, **5**, 7282.
49 L. Zhang, T. Wang, L. Li, C. Wang, Z. Su and J. Li, *Chem. Commun.*, 2012, **48**, 8706.
50 L. Xing, Y. Cao and S. Che, *Chem. Commun.*, 2012, **48**, 5995.
51 H. Liu, D. Chen, L. Li, T. Liu, L. Tan, X. Wu and F. Tang, *Angew. Chem., Int. Ed.*, 2011, **50**, 891.

